

Article

A Novel and Compact Slotted-Decahedral Antenna for 5G Devices

Karen Nallely Olan Nuñez  and Roberto S. Murphy Arteaga * 

Electronics Department, Instituto Nacional de Astrofísica, Óptica y Electrónica (INAOE), Tonantzintla, Puebla 72840, Mexico; karen.olan@inaoep.mx

* Correspondence: rmurphy@ieee.org; Tel.: +52-222-736-9044

Abstract: In this paper, a compact SISO (Single-Input Single-Output) antenna with a novel slotted-decahedral geometry is presented. The design was performed using a full-wave simulator (FWS). A decahedral patch with an eight-pointed star-shaped slot and two rectangular grooves is the main characteristic of the proposed novel radiator. The decagon shape, eight-pointed star-shaped slot, rectangular grooves, and separate section give rise to radiation. The SISO antenna operates from 23.1 to 29.94 GHz covering the proposed frequency bands for 5G wireless communication systems. The radiation pattern stability, moderate to high gain values (6.5 dBi, average), good radiation efficiency (higher than 89.4%), wide impedance bandwidth (6.84 GHz), compactness ($13 \times 13 \times 0.787 \text{ mm}^3$) and ease of manufacture are the principles advantages of this novel geometry. The experimental validation of the SISO antenna was performed, and good agreement was obtained with simulation results, and an equivalent circuit model was proposed. The proposed SISO antenna can be easily integrated into wireless sensors, drones, backhaul, and 5G devices which support IoT, working in the n257, n258 and n261 frequency bands.

Keywords: 5G; antennas; SISO antennas; n257; n258; n261



Citation: Olan Nuñez, K.N.; Murphy Arteaga, R.S. A Novel and Compact Slotted-Decahedral Antenna for 5G Devices. *Electronics* **2022**, *11*, 1813. <https://doi.org/10.3390/electronics11121813>

Academic Editors: Faisal Tubbal, Ladislau Matekovits and Raad Raad

Received: 19 May 2022

Accepted: 30 May 2022

Published: 7 June 2022

Publisher's Note: MDPI stays neutral with regard to jurisdictional claims in published maps and institutional affiliations.



Copyright: © 2022 by the authors. Licensee MDPI, Basel, Switzerland. This article is an open access article distributed under the terms and conditions of the Creative Commons Attribution (CC BY) license (<https://creativecommons.org/licenses/by/4.0/>).

1. Introduction

Nowadays, the 5G standard of communications is ubiquitous and pervasive, taking every day more importance for our daily lives. And we can be sure that its impact will continue to grow, as there are more devices and applications that require the signal transfer quality that this network can offer. Moreover, human endeavor is shifting toward the Internet of Things (IoT), also called the Internet of Everything (IoE), to provide, control, and monitor a slew of routinely activities in the fields of personal and commercial communications, industry, health services, banking, safety, education, and entertainment, to mention just a few [1,2].

The initial 5G network operating bands are divided into two sub-bands, called FR1 and FR2 (for Frequency Range). The first consists of a host of assigned frequencies between 450 MHz and 6 GHz, thus also dubbed “the sub 6 GHz band”. The second one comprises allocated frequencies between 24.25 to 52.6 GHz [3–7]. In this one, the frequencies that are being exploited cover the n257 (26.50 GHz to 29.50 GHz), n258 (24.25 GHz to 27.50 GHz), and the n261 (27.50 GHz to 28.35 GHz) sub-bands. Some of the antennas designed for FR1, however, are the basis for those used for FR2 [8–10]. In this frequency range, special attention has been placed for applications around 28 GHz, since it can operate with a broader bandwidth [11].

This paper focuses on the design of a Single Input Single Output (SISO) antenna to cover the needs for devices using the frequency bands from 24.25 GHz to 29.50 GHz. In fact, the antenna was designed, simulated, fabricated, and measured, demonstrating a very good response from 23.1 GHz to 29.94 GHz.

Moreover, this antenna can be used as the basis for Multiple Input Multiple Output (MIMO) systems. MIMO allows for size optimization, broader bandwidth, stable radiation

patterns and higher gains, among other fundamental figures of merit [12–24]. These, however, require careful design considerations, especially related to coupling. This has become a very important field of endeavor, tackled by many researchers around the world [25–33].

The paper is organized as follows. Section 2 details the antenna design process, based on full wave simulations. Experimental results are presented and discussed in Section 3. Section 4 presents a discussion of the results, compared to similar recently reported structures. The paper closes with general conclusions, presented in Section 5.

2. Materials and Methods

The proposed novel geometry, named “slotted-decahedral antenna”, is shown in Figure 1, which includes its geometrical design parameters.

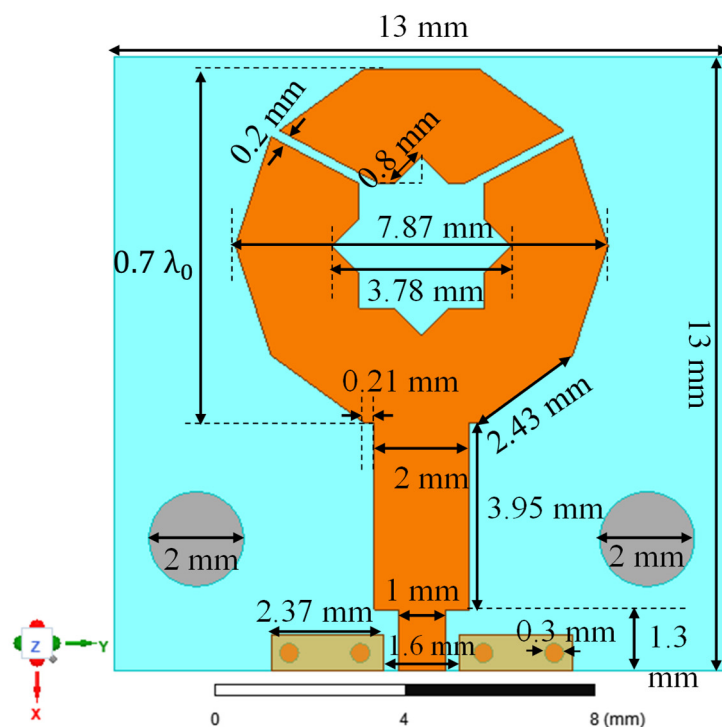


Figure 1. Proposed novel geometry and design parameters.

The geometry is based on a decahedral patch with an eight-pointed star-shaped slot at its center, and two rectangular grooves at the end of the radiator, which enhance stability in the shape of the radiation pattern across the impedance bandwidth (from 23 GHz to 29.9 GHz) through its resonating response. A commercial Rogers 4350B substrate was used for the proposed antenna design, which has a thickness of 0.787 mm, a loss tangent δ of 0.004 and a relative dielectric constant (ϵ_r) of 3.66.

The width of the feed line (1 mm) and the spacing between the feed line and top ground (0.3 mm) were chosen considering connector dimensions. The 2 mm wide line has a characteristic impedance of 50Ω to achieve impedance matching.

The structure was defined on a full-wave simulator, including as many material, geometrical and process-related parameters as possible. This structure is shown in Figure 2, a render that is very close to the real structure.

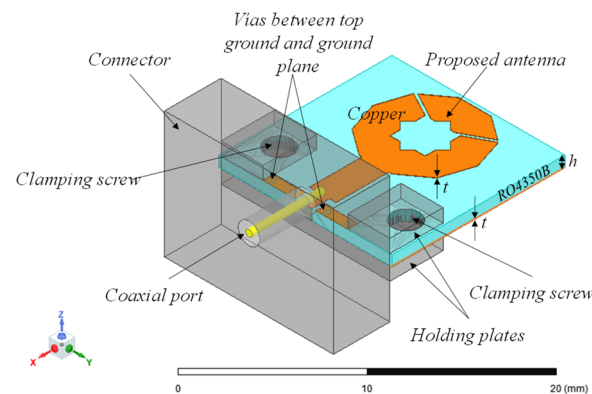


Figure 2. Antenna structure defined in the full-wave simulator, including the connector ($h = 0.787$ mm, $t = 17.5$ μ m).

The design evolution and a comparison of four important figures of merit during the design process is shown in Figure 3, step #5 being the final design. Figure 3a illustrates the five design steps; (b) the reflection coefficient at the input port, using a reference impedance of 50 Ω ; (c) the behavior of peak gain and radiation efficiency for every design step; and (d), the radiation patterns obtained for each design step. Something that is noteworthy in this figure is the change in shape of the radiation pattern, that is, each design step causes the pattern to become more directive and more symmetrical.

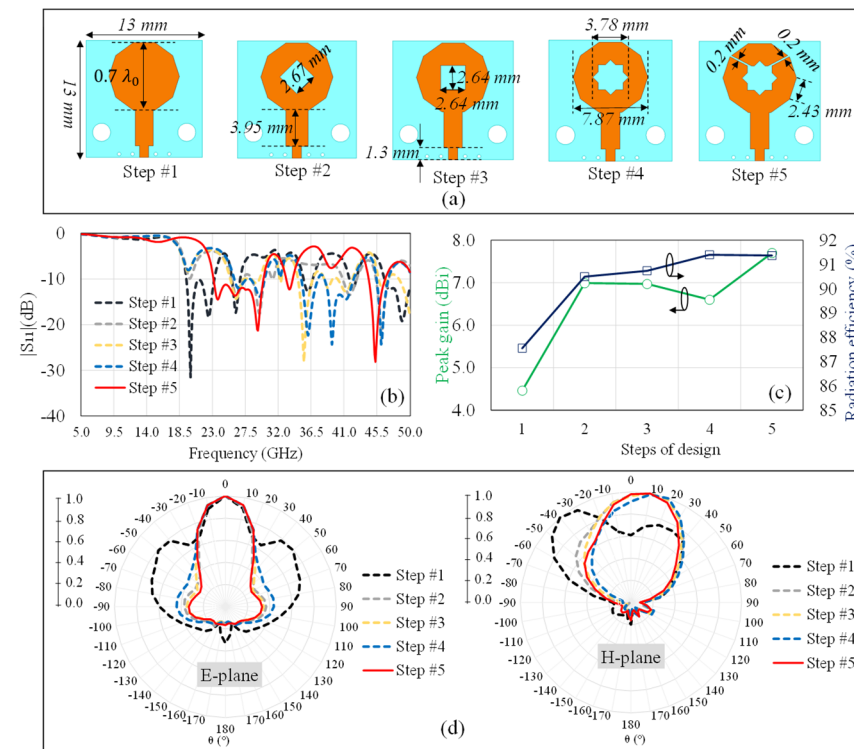


Figure 3. Design evolution and comparison of (a) Steps of the design process and antenna dimensions; (b) Return loss; (c) Peak gains and radiation efficiencies at 28 GHz; and (d) 2D—normalized radiation patterns at 28 GHz.

During the design process different shapes for the antenna were tested, as well as different shapes for the slots. Figure 4 shows six 3D-radiation patterns from the full-wave simulator. The same figure contains squares and ellipses highlighting the points where the radiation is the least intense.

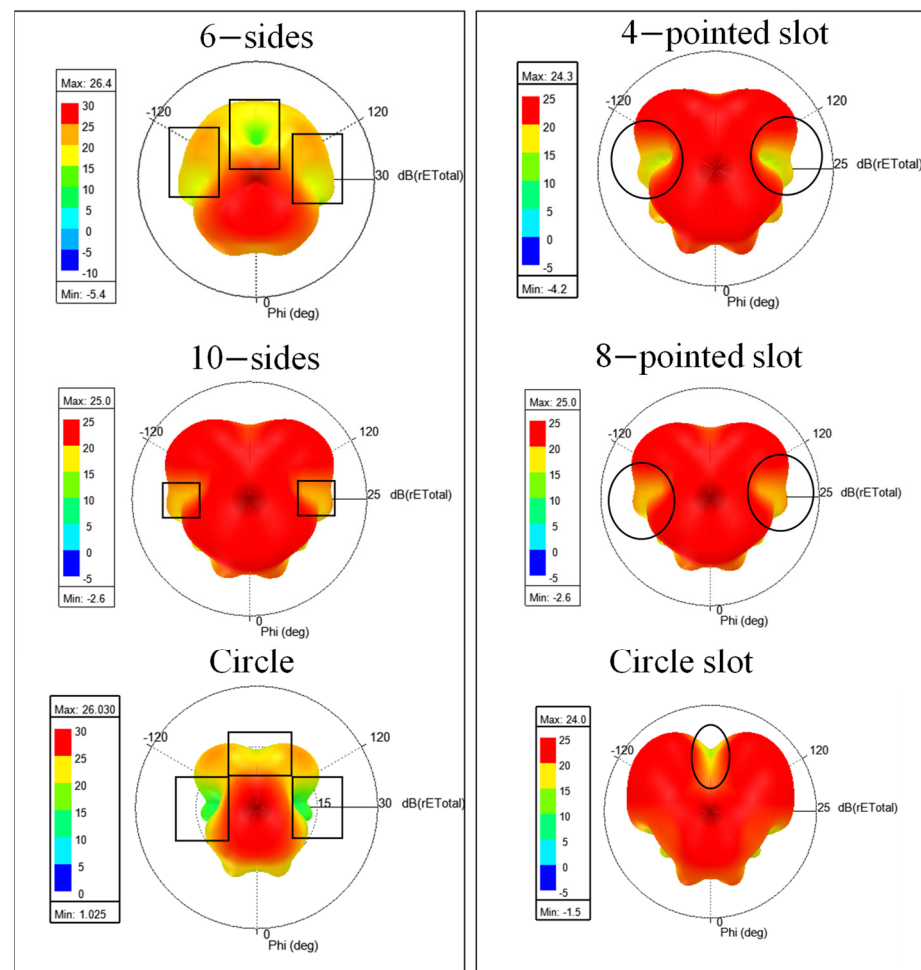


Figure 4. 3D—radiation patterns (in dB) from simulation, at the left—side of different antenna shape, and at the right-side of different slot shape.

The best performance, considering the radiation pattern shape, gain, radiation efficiency and impedance bandwidth, is obtained when the antenna shape is 10 sided and the slot is 8-pointed, herein named “eight-pointed star-shaped slot”.

To verify the working principle, the electric and magnetic fields were plotted; these graphs are shown in Figure 5. At the lower frequency, 23 GHz, resonance is mainly due to the decagon shape and rectangular grooves.

In the medium frequency range and beyond—that is 28 GHz to 30 GHz—some other effects occur. When the fields reach the rectangular grooves, Figure 6, the magnetic field (B_i) induces an electromotive force (induced EMF) in the separate section. The induced EMF gives rise to a magnetic field (B_{EMF}) going in the opposite direction, propagating in this small separate section of the antenna. This occurs when the phase of the magnetic field reaches its first positive half-cycle maximum (phase = 90°). On the contrary, when the second maximum of the negative half cycle occurs (phase = 270°) the magnetic field produced in the separate section now goes in the opposite direction than that generated with the 90° phase. This change in the direction of magnetic field happens continuously, since the phase of the electromagnetic wave changes as it propagates. Moreover, the electric field (associated to the induced EMF, E_{EMF}) in the separate section also causes this section to enter a state of resonance. Furthermore, the initial electric field (from the excitation pathway, E_i) is cancelled at the rectangular opening. At the same time, around 28 GHz and 30 GHz, the eight-pointed star-shaped slot at the center, becomes resonant.

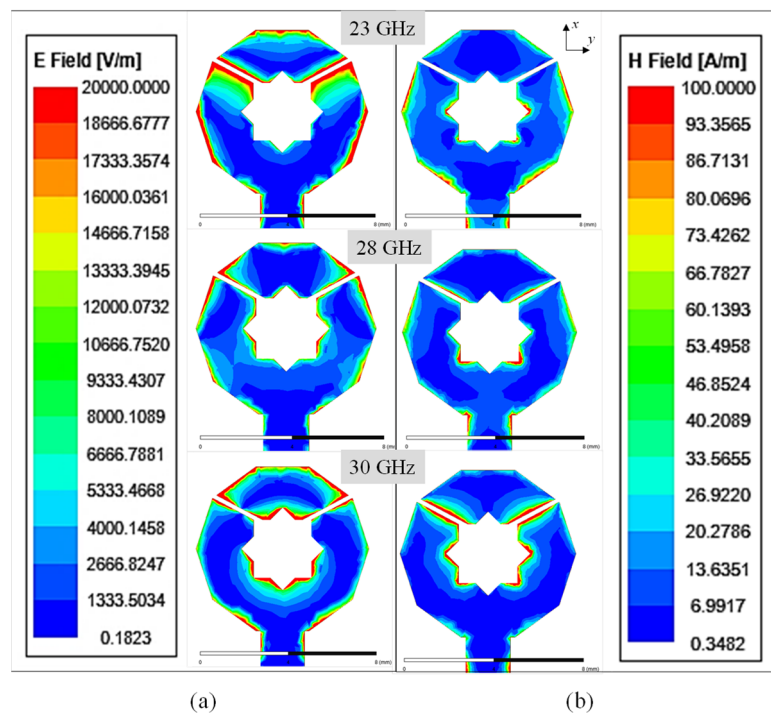


Figure 5. (a) Electric field (b) magnetic field (in magnitude) plotted in the upper layer of the metal at 23 GHz, 28 GHz, and 30 GHz.

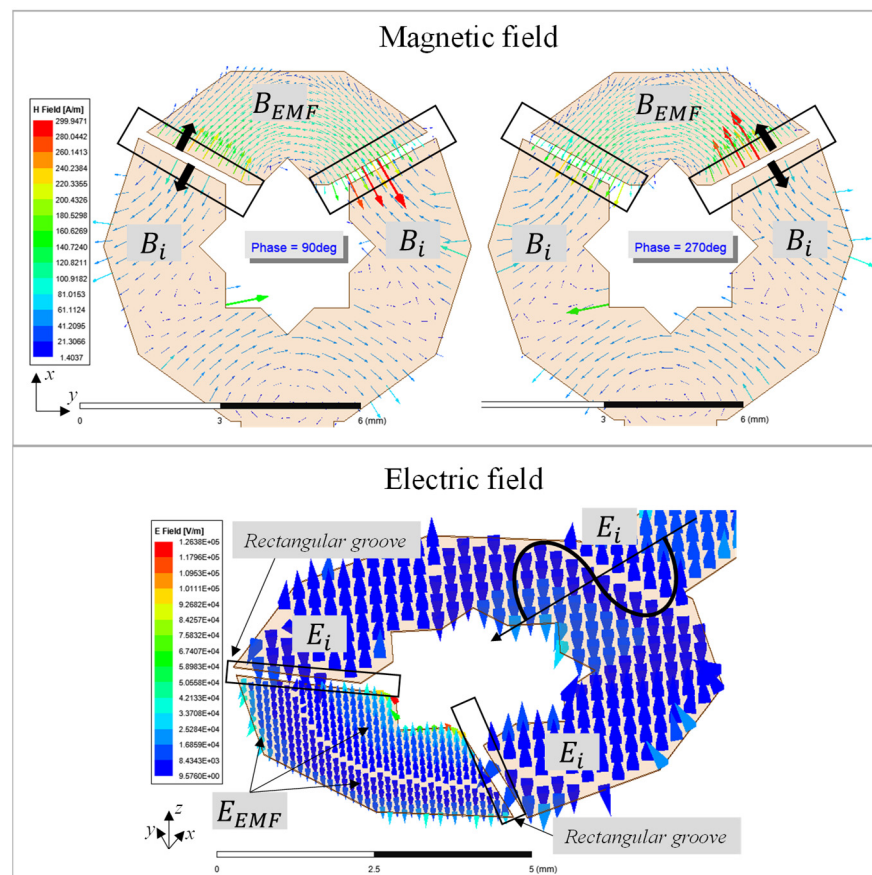


Figure 6. Magnetic and electric fields around the rectangular grooves.

On the other hand, the 33 GHz and 45 GHz frequency bands from $|S_{11}|$ in Figure 3a (step#5), are generated by the 8-pointed star slot, at its center, and by the two rectangular grooves. However, when analyzing some radiation parameters, such as, radiation efficiency, gain, and radiation pattern, the structure presents some nulls and secondary lobes, such as Figure 7 shows. Besides, the radiation efficiency is about 84% and 91% at 33 and 45 GHz, respectively. In consequence, these bands are not considered in the bandwidth of the novel proposed SISO antenna.

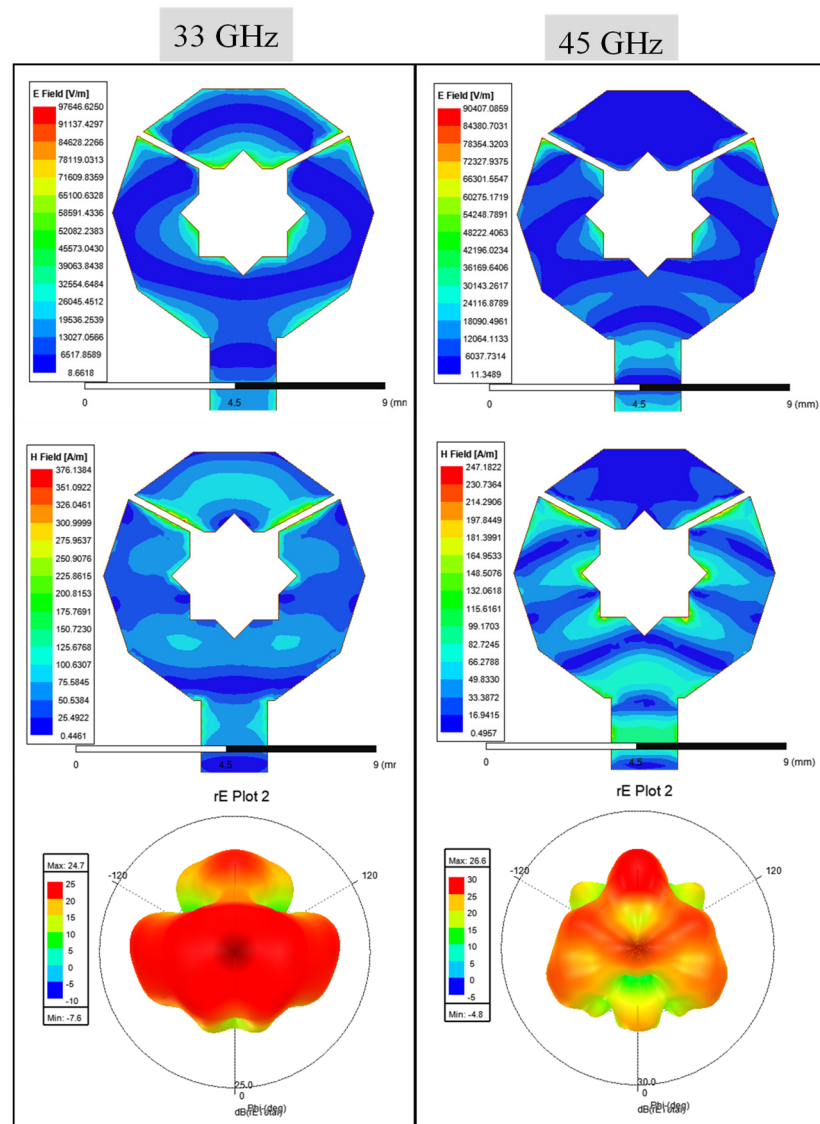


Figure 7. Magnetic and electric fields (in magnitude) and 3D—radiation patterns (in dB) at 33 and 45 GHz, respectively.

3. Results

To verify that the proposed design performs correctly in the frequency band from 23.1 to 29.94 GHz, apt for 5G technologies, the antenna was fabricated and measured. Its performance was then assessed from measured and simulated results.

A photograph of the fabricated antenna, including connectors, is presented as Figure 8a,b. The challenge in the manufacture of this prototype was making the perforations in the substrate to be able to use the connector, as well as the paths from the upper ground to the lower ground plane.

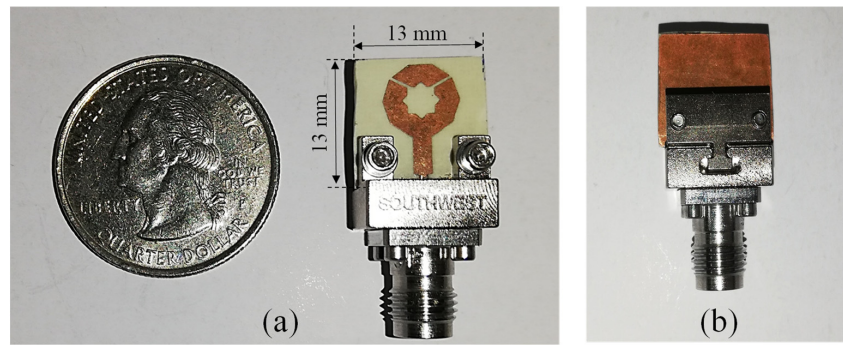


Figure 8. Fabricated antenna; (a) Front view, and (b) back view.

The measurements were performed using an Anritsu Vector Network Analyzer (VNA), in conjunction with an automatic calibration device (Autocal 36585 V). Figure 9 shows the experimental setup.

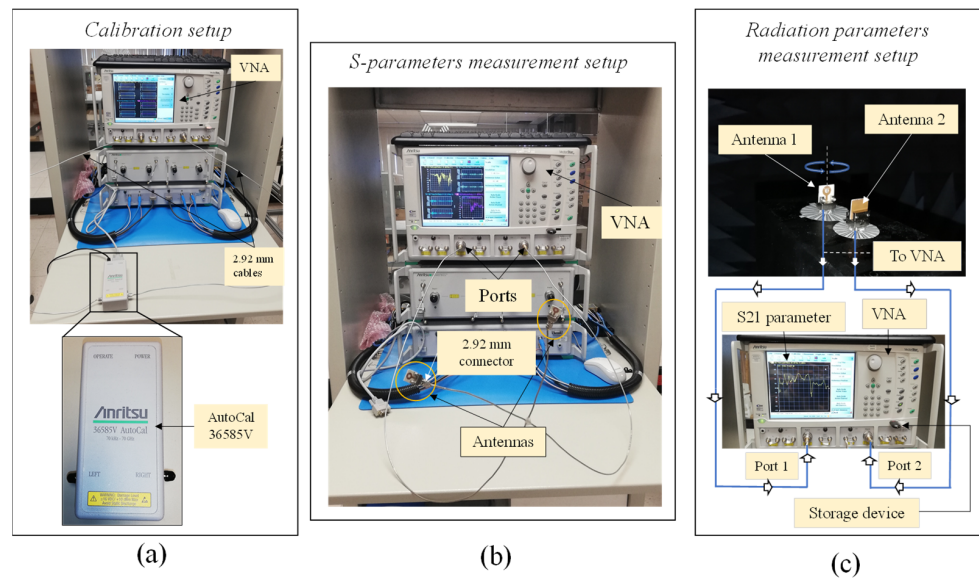


Figure 9. Measurement setup to (a) calibration, (b) S-parameters, and (c) radiation test.

The return loss at the input port from simulation and measurement is shown in Figure 10a. Moreover, the same figure shows a small frequency shift (600 MHz and 550 MHz) between measurement and simulation, which does affect the operating bandwidth.

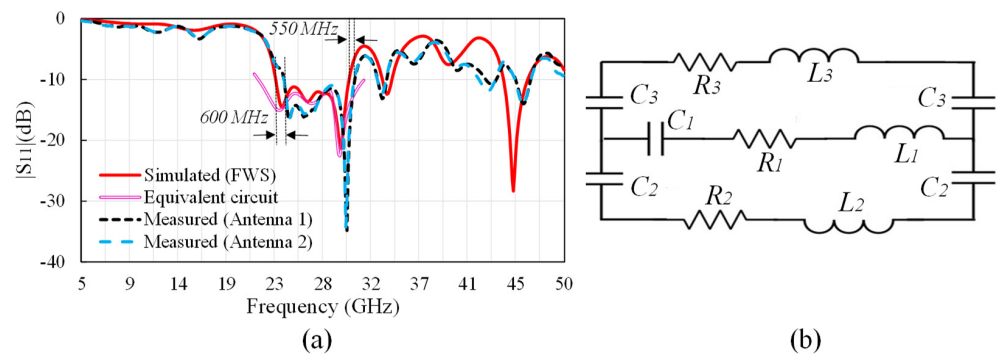


Figure 10. (a) Comparison of theoretical (using a full—wave simulator, FWS), equivalent circuit, and experimental reflection coefficient at the input port of the proposed design; and (b) the proposed equivalent circuit suitable for the 23 to 30 GHz frequency range.

In order to measure the radiation pattern, two antennas were built to determine the appropriate parameters following the methodology described in [34], which requires the two antennas to be identical. As can be seen on Figure 10a, the response of the two antennas is practically identical in the frequency range of interest, and thus we can conclude that they behave as identical electrically.

Additionally, a proposed equivalent circuit is shown in Figure 10b. The lumped elements represent the multiple phenomena occurring in this frequency range, and the model is seen to have a good correlation with full-wave simulation (FWS) results, carried out in Ansys Electronics' HFSS. The values of the proposed model are $R_1 = 10.29 \Omega$, $R_2 = 29 \Omega$, $R_3 = 30.2 \Omega$, $L_1 = 3 \text{ nH}$, $L_2 = 2.22 \text{ nH}$, $L_3 = 1.45 \text{ nH}$, $C_1 = 0.01 \text{ pF}$, $C_2 = 0.04 \text{ pF}$, and $C_3 = 0.049 \text{ pF}$. Such values were obtained through an optimization process using ADS (Advance Design System, version 2022) simulations. Here, C_2 and C_3 represent the rectangular grooves. R_1 - L_1 - C_1 correspond to the response around 23 GHz, R_2 - L_2 - C_2 to that around 26.5 GHz, and R_3 - L_3 - C_3 account for the response about 29.7 GHz. All together, they model the behavior of the antenna from 23 to 30 GHz.

The measured and simulated 2D-radiation patterns are graphed in Figure 11, while the gain values across the impedance bandwidth are shown in Figure 12.

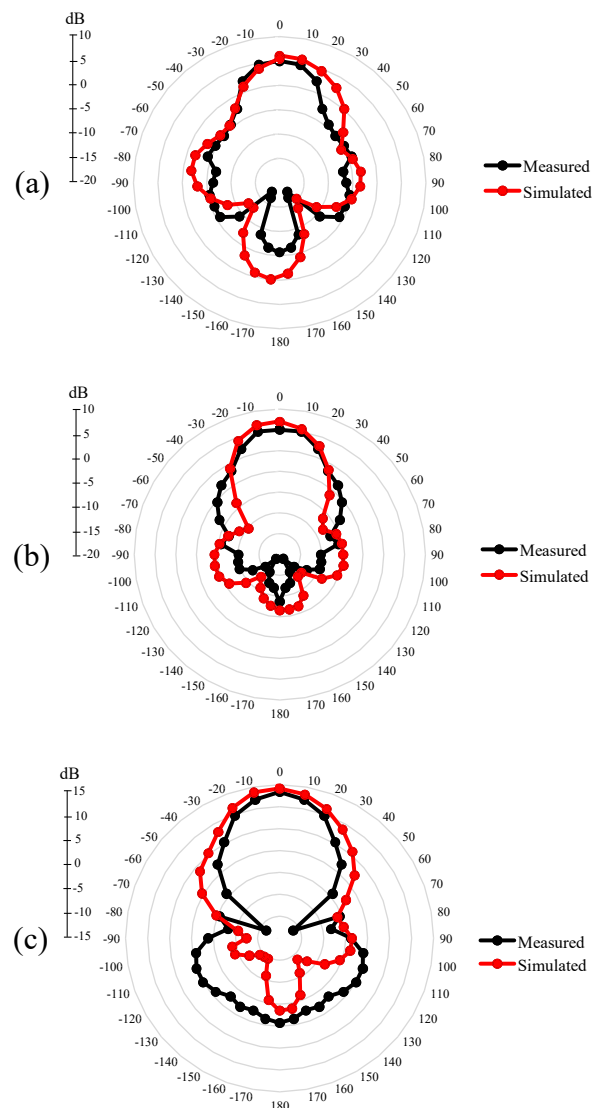


Figure 11. 2D—Normalized radiation patterns at (a) 23 GHz, (b) 28 GHz, and (c) 30 GHz from simulation and measurement.

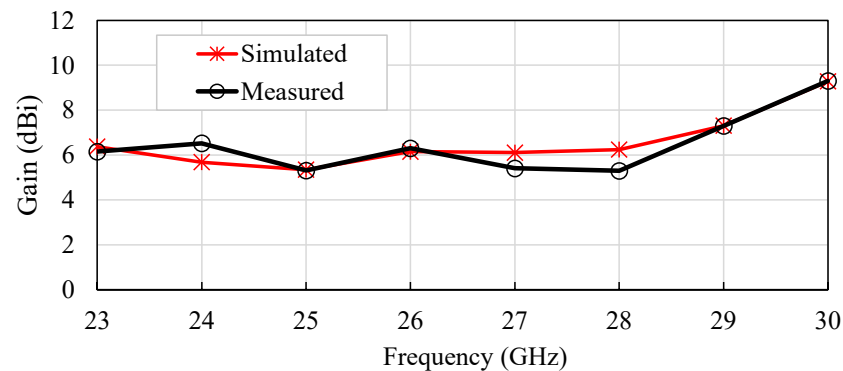


Figure 12. Measured and simulated gains from 23 to 30 GHz at $\theta = 0^\circ$.

Once the performance of the proposed SISO antenna has been tested and validated, its principal figures of merit were determined to compare it with related works. This comparison is summarized in Table 1.

The proposed design has a compact size, which makes it suitable for integration into compact 5G devices that support IoT, and presents a wide impedance bandwidth covering the n257, n258, and n261 bands.

The gain values in Figure 12 are above 6 dBi at 24 GHz and up to 9.2 dBi at 29.9 GHz, from simulation, and above 5 dBi and up to 9 dBi from measurement. It is important to note that these values are high considering they were obtained with a single radiating element (SISO antenna).

The cross-polarization and co-polarization, in dB, are shown in Figure 13, from the full-wave simulator, the co-pol values are higher than 0 dB and the cross-pol values are around -40 dB.

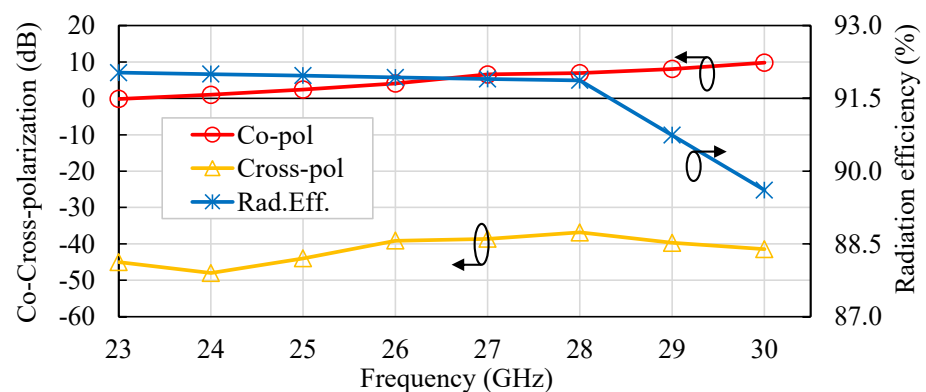


Figure 13. Co-polarization, cross-polarization, and radiation efficiency over the bandwidth of operation.

The radiation efficiency is also shown in Figure 13; it was obtained from the full-wave simulation, considering finite conductivity, the loss coefficient of the substrate, and other effects, such as mismatching of impedances of the proposed antenna and the connector's impedance across the impedance bandwidth, as well as the coupling between the holding plates and the antenna. The values are better than 89% (at 29.9 GHz) and up to 92% (at 24 GHz).

The radiation efficiency is reduced when including the connector during the simulation: 8% less at 23.1 GHz, 7% less at 28 GHz, and 9% less at 29.9 GHz. Besides, the shape of the radiation pattern is affected by the connector (holding plates and backplane).

Although during the simulations many parameters were considered, some others cannot be predicted and added to the simulation, such as imperfections in the metal of the radiator element, reduction of the metal layer during manufacture, small differences in the thickness of the substrate, imperfections inherent to the substrate, reflections due to the

size of the connector being comparable to the size of the antenna, as well as random errors due to setup calibration, cable attenuation (1.96–2.32 dB/m [35]), and misalignment of the device under test.

We thus attribute the difference in gain between experimental and simulation results, shown in Figure 12, to these effects.

Despite obtaining lower gains during the experimental validation, we believe that the attained gain values are good, since they have a similar behavior to those of simulation, and they are higher than 5 dBi throughout the impedance bandwidth. The average gain from measurement is 6.44 dBi whereas the simulated one is 6.56 dBi.

The radiation patterns show good correlation with the simulated patterns. These have one only beam, normal to the decahedral geometry, and an HPBW close to 40°.

The back lobes (in the three patterns) are apparently large, but this is only an appreciation, these lobes have lower values than the principal beam.

4. Discussion

Considering the recent 5G developments regarding antennas, a comparison with reported works for the same frequency band for 5G technology above of 6 GHz (5G mm-wave frequency band) is shown in Table 1.

It should be noted that this table contains two types of SISO (Single-Input Single-Output) antennas, for a fair comparison; SISO antennas of a single element [36,37] and SISO antennas of multiple elements [38–40].

Moreover, is important to highlight that the listed designs are the most recent developments (2020–2021).

The antenna herein proposed has many advantages when compared with [36], such as higher gain, higher radiation efficiency, higher bandwidth, and compactness.

The designs presented by [38–40] have higher gains than our proposal, but it is important to note that those works are arrays of elements. Thus, it is reasonable to expect higher gains.

Our design bests that of [38] in impedance bandwidth, HPBW, and above all, it is much more compact.

With respect to [39], the proposed design in this work is better in impedance bandwidth, HPBW, radiation efficiency, and volume (considering that it requires two substrate layers).

Furthermore, the design presented by [40] requires two substrate layers, and the total area is large compared with our work. That work, however, attains good values of gain, impedance bandwidth, and polarization.

A single element antenna is reported in [37], but it has a narrow bandwidth of just 1.5 GHz. Despite having a high gain value this design is large (19 times larger than ours), and its HPBW is narrow.

Table 1. Comparison with Related Works Operating at 28 Ghz (SISO Antennas).

Parameter	Work					
	[36]	[38]	[39]	[40]	[37]	This Work
Substrate and thickness (h)	Rogers 5880 h = 0.787 mm	Rogers RT/Duroid 5880 h = 0.52 mm	Rogers Duroid RT5880 h1 = 0.5 mm h2 = 0.8 mm	Rogers 5880 h1 = 1 mm h2 = 0.508 mm	Rogers RT/Duroid 5880 h = 0.127 mm	Rogers 4350 B h = 0.787 mm
Total area (mm ²) (λ ₀ at 28 GHz)	21.9 × 5.64 2.05 λ ₀ × 0.53 λ ₀	75 × 100 7 λ ₀ × 9.34 λ ₀	34 × 36 3.18 λ ₀ × 3.36 λ ₀	~ 40 × 40 3.74 λ ₀ × 3.74 λ ₀	48 × 67 4.48 λ ₀ × 6.26 λ ₀	13 × 13 1.21 λ ₀ × 1.21 λ ₀
Design type	Antipodal Vivaldi antenna	2 × 2 Patch array	2 × 2 Dual off-center-fed dipoles (array)	Magneto-electric dipole 1 × 2 array	Reconfigurable Leaky-wave antenna based on a HMSIW	Single element antenna based on decahedral geometry
Reflection coefficient	−25 dB	~−18 dB	~−15 dB	~−15 dB	~−15 dB	−21.5 dB

Table 1. Cont.

Work Parameter	[36]	[38]	[39]	[40]	[37]	This Work
Impedance bandwidth	4.66 GHz (28 GHz band)	720 MHz (27.75–28.47 GHz)	3 GHz (27.2–30.2 GHz)	7 GHz (24.4–31.4 GHz)	1.5 GHz (28–29.5 GHz)	6.84 GHz (23.1–29.94 GHz)
Gain	3.4 dBi 3.6 dBi 7.4 dBi	9.97 dBi 12.3 dBi	13.1 dBi 13.2 dBi	10 dBic	8.2 ± 0.6 dBi	6.56 dBi Average
Polarization	N.A.	Linear	Dual linear	Circular	N.A.	Linear
Radiation efficiency	>86% (28 GHz band)	>96% (28 GHz band)	88% (28 GHz band)	N.A.	N.A.	>89.4%
HPBW	266° (E-plane) 160° (H-plane)	29.9° (E-plane) 60.0° (H-plane)	12° (xz-plane) 11° (yz-plane)	N.A.	29°	40° (E-plane) 65° (H-plane)
Operation frequencies	14.44–20.98 GHz 24.34–29 GHz 33–40 GHz	5.9 GHz 28 GHz	28 GHz 38 GHz	28 GHz bands	28 GHz band	28 GHz bands
Design complexity	high	low	high	high	medium	medium
Fabrication	Easy	Easy	Difficult	Difficult	Easy	Easy

N.A. is Not Available. HMSIW is Half-Mode Substrate Integrated Waveguide. HPBW is Half Power Beam Width.

5. Conclusions

In this paper we present a novel antenna design based on a decahedral patch with an eight-pointed star-shaped slot and two rectangular grooves at the end of the radiator.

This design has a very compact size ($13 \times 13 \times 0.787 \text{ mm}^3$), wide impedance bandwidth (6.84 GHz) covering the proposed bands for 5G technology, above 6 GHz (n257, n258, and n261), specifically from 23.1 GHz to 29.9 GHz, stable radiation pattern, average gain of 6.56 dBi (values from 5.3 dBi to 9.28 dBi), and radiation efficiency better than 89%, from simulation.

The performance of the proposed novel geometry (SISO antenna) is suitable for compact 5G devices that support IoT. The experimental validation was performed, showing a very good agreement with simulation results, especially in return loss, gain and radiation pattern.

Author Contributions: K.N.O.N. conceived the idea, designed the structure, and wrote the principal ideas. R.S.M.A. revised the manuscript, contributed some ideas, and supervised the work. All authors have read and agreed to the published version of the manuscript.

Funding: This research was funded by CONACyT, México, under grant numbers 852217 and 285199.

Institutional Review Board Statement: Not applicable.

Informed Consent Statement: Not applicable.

Data Availability Statement: Not applicable.

Conflicts of Interest: The authors declare no conflict of interest.

References

- Andrews, J.G.; Buzzi, S.; Choi, W.; Hanly, S.V.; Lozano, A.; Soong, A.C.K.; Zhang, J.C. What will 5G be? *IEEE J. Sel. Areas Commun.* **2014**, *32*, 1065–1082. [[CrossRef](#)]
- Attiah, M.L.; Isa, A.; Zakaria, Z.; Abdulhameed, M.; Mohsen, M.K.; Ali, I. A survey of mmWave user association mechanisms and spectrum sharing approaches: An overview, open issues and challenges, future research trends. *Wirel. Netw.* **2020**, *26*, 2487–2514. [[CrossRef](#)]
- Kumar, S.; Dixit, A.S.; Malekar, R.R.; Raut, H.D.; Shevada, L.K. Fifth Generation Antennas: A Comprehensive Review of Design and Performance Enhancement Techniques. *IEEE Access* **2020**, *8*, 163568–163593. [[CrossRef](#)]
- Guidelines for Evaluation of Radio Interface Technologies for IMT-2020*; Document ITU-R M.2412-0; International Telecommunication Union: Geneva, Switzerland, 2017; pp. 1–144.
- Requirements, Evaluation Criteria and Submission Templates for the Development of IMT-2020*; Document Report ITU-R M.2411-0; International Telecommunication Union: Geneva, Switzerland, 2017; pp. 1–32.

6. Zhao, A.; Ren, Z. Wideband MIMO antenna systems based on coupled-loop antenna for 5G N77/N78/N79 applications in mobile terminals. *IEE Access* **2019**, *7*, 93761–93771. [[CrossRef](#)]
7. *Technical Feasibility of IMT in Bands Above 6 GHz*; Document ITU-R M.2376-0; International Telecommunication Union: Geneva, Switzerland, 2015; pp. 1–134.
8. Abdullah, M.; Altaf, A.; Anjum, M.R.; Arain, Z.A.; Jamal, A.A.; Alibakhshikenari, M.; Falcone, F.; Limiti, E. Future Smartphone: MIMO Antenna System for 5G Mobile Terminals. *IEEE Access* **2021**, *9*, 91593–91603. [[CrossRef](#)]
9. Kiani, S.H.; Altaf, A.; Anjum, M.R.; Afridi, S.; Arain, Z.A.; Anwar, S.; Khan, S.; Alibakhshikenari, M.; Lalbakhsh, A.; Khan, M.A.; et al. MIMO Antenna System for Modern 5G Handheld Devices with Healthcare and High Rate Delivery. *Sensors* **2021**, *21*, 7415. [[CrossRef](#)]
10. Khalid, H.; Awan, W.A.; Hussain, M.; Fatima, A.; Ali, M.; Hussain, N.; Khan, S.; Alibakhshikenari, M.; Limiti, E. Design of an Integrated Sub-6 GHz and mmWave MIMO Antenna for 5G Handheld Devices. *Appl. Sci.* **2021**, *11*, 8331. [[CrossRef](#)]
11. Rappaport, T.S.; Xing, Y.; MacCartney, G.R.; Molisch, A.F.; Mellios, E.; Zhang, J. Overview of millimeter wave communications for fifth generation (5G) wireless networks with a focus on propagation models. *IEEE Trans. Antennas Propag.* **2017**, *65*, 6213–6230. [[CrossRef](#)]
12. Xi, L. A wideband planar filtering dipole antenna for 5G communication applications. *Microw. Opt. Technol. Lett.* **2019**, *61*, 2746–2751. [[CrossRef](#)]
13. Hussain, N.; Jeong, M.J.; Abbas, A.; Kim, T.J.; Kim, N. A metasurface-based low-profile wideband circularly polarized patch antenna for 5G millimeter-wave systems. *IEEE Access* **2020**, *8*, 22127–22135. [[CrossRef](#)]
14. Zeng, J.; Luk, K.-M. Single-layered broadband magnetolectric dipole antenna for new 5G application. *IEEE Antennas Wirel. Propag. Lett.* **2019**, *18*, 911–915. [[CrossRef](#)]
15. Karthikeya, G.S.; Abegaonkar, M.P.; Koul, S.K. A wideband conformal antenna with high pattern integrity for mmWave 5G smartphones. *Prog. Electromagn. Res. Lett.* **2019**, *84*, 1–6. [[CrossRef](#)]
16. Desai, A.; Upadhyaya, T.; Patel, R. Compact wideband transparent antenna for 5G communication systems. *Microw. Opt. Technol. Lett.* **2019**, *61*, 781–786. [[CrossRef](#)]
17. Alkaraki, S.; Andy, A.S.; Gao, Y.; Tong, K.-F.; Ying, Z.; Donnan, R.; Parini, C. Compact and low-cost 3-D printed antennas metalized using spray-coating technology for 5G mm-Wave communication systems. *IEEE Antennas Wirel. Propag. Lett.* **2018**, *17*, 2051–2055. [[CrossRef](#)]
18. Yin, J.; Wu, Q.; Yu, C.; Wang, H.; Hong, W. Broadband endfire magnetolectric dipole antenna array using SICL feeding network for 5G millimeter-wave applications. *IEEE Trans. Antennas Propag.* **2019**, *67*, 4895–4900. [[CrossRef](#)]
19. Mujammami, E.H.; Sebak, A.B. Wideband high gain printed quasi-Yagi diffraction gratings-based antenna for 5G applications. *IEEE Access* **2019**, *7*, 18089–18100. [[CrossRef](#)]
20. Dzagbletey, P.A.; Jung, Y.-B. Stacked microstrip linear array for millimeter-wave 5G baseband communication. *IEEE Antennas Wireless Propag. Lett.* **2018**, *17*, 780–783. [[CrossRef](#)]
21. Goel, T.; Patnaik, A. Novel broadband antennas for future mobile communications. *IEEE Trans. Antennas Propag.* **2018**, *66*, 2299–2308. [[CrossRef](#)]
22. Kim, E.; Ko, S.T.; Lee, Y.J.; Oh, J. Millimeter-wave tiny lens antenna employing U-shaped filter arrays for 5G. *IEEE Antennas Wireless Propag. Lett.* **2018**, *17*, 845–848. [[CrossRef](#)]
23. Wen, B.J.; Peng, L.; Li, X.F.; Mo, K.S.; Jiang, X.; Li, S.M. A low profile and wideband unidirectional antenna using bandwidth enhanced resonance-based reflector for fifth generation (5G) systems applications. *IEEE Access* **2019**, *7*, 27352–27361. [[CrossRef](#)]
24. Feng, B.; Li, L.; Zeng, Q.; Chung, K.L. A wideband antenna using metasurface for the 2G/3G/LTE/5G communications. *Microw. Opt. Technol. Lett.* **2018**, *60*, 2482–2487.
25. Nadeem, I.; Choi, D.-Y. Study on mutual coupling reduction technique for MIMO antennas. *IEEE Access* **2019**, *7*, 563–586. [[CrossRef](#)]
26. Sharawi, M.S.; Podilchak, S.K.; Khan, M.U.; Antar, Y.M. Dual frequency DRA-based MIMO antenna system for wireless access points. *IET Microw., Antennas Propag.* **2017**, *11*, 1174–1182. [[CrossRef](#)]
27. Zhang, Y.; Deng, J.-Y.; Li, M.-J.; Sun, D.; Guo, L.-X. A MIMO dielectric resonator antenna with improved isolation for 5G mm-Wave applications. *IEEE Antennas Wireless Propag. Lett.* **2019**, *18*, 747–751. [[CrossRef](#)]
28. Kowalewski, J.; Eisenbeis, J.; Jauch, A.; Mayer, J.; Kretschmann, M.; Zwick, T. A mmW broadband dual-polarized dielectric resonator antenna based on hybrid modes. *IEEE Antennas Wirel. Propag. Lett.* **2020**, *19*, 1068–1072. [[CrossRef](#)]
29. Alibakhshikenari, M.; Khalily, M.; Virdee, B.S.; See, C.H.; Abd-Alhameed, R.A.; Limiti, E. Mutual Coupling Suppression between Two Closely Placed Microstrip Patches Using EM-Bandgap Metamaterial Fractal Loading. *IEEE Access* **2019**, *7*, 23606–23614. [[CrossRef](#)]
30. Alibakhshikenari, M.; Khalily, M.; Virdee, B.S.; See, C.H.; Abd-Alhameed, R.A.; Limiti, E. Mutual-Coupling Isolation Using Embedded Metamaterial EM Bandgap Decoupling Slab for Densely Packed Array Antennas. *IEEE Access* **2019**, *7*, 51827–51840. [[CrossRef](#)]
31. Jamshidi, M.B.; Roshani, S.; Talla, J.; Roshani, S.; Peroutka, Z. Size reduction and performance improvement of a microstrip Wilkinson power divider using a hybrid design technique. *Sci. Rep.* **2021**, *11*, 7773. [[CrossRef](#)]
32. Roshani, S.; Roshani, S. A compact coupler design using meandered compact microstrip resonant cell (MLCMRC) and bended lines. *Wirel. Netw.* **2021**, *27*, 677–684. [[CrossRef](#)]

33. Li, Y.; Sim, C.-Y.-D.; Luo, Y.; Yang, G. 12-port 5G massive MIMO antenna array in sub-6 GHz mobile handset for LTE bands 42/43/46 applications. *IEEE Access* **2018**, *6*, 344–354. [[CrossRef](#)]
34. Medina, J.L.; Díaz, E.; Olera, J.L.; Chávez, R.A.; Velázquez, A. Análisis y Comparación de Metodologías Para Determinar Experimentalmente la Ganancia de Antenas de RF Y Microondas. In Proceedings of the Metrology Symposium, Querétaro, Mexico, 22 October 2008.
35. Huber+Suhner. Formable Microwave Cable: SR_118_TP. Data Sheet. Available online: <https://ecatalog.hubersuhner.com/media/documents/datasheet/en/pdf/22810073> (accessed on 26 May 2022).
36. Ullah, R.; Ullah, S.; Faisal, F.; Ullah, R.; Choi, D.Y.; Ahmad, A.; Kamal, B. High-Gain Vivaldi Antenna with Wide Bandwidth Characteristics for 5G Mobile and Ku-Band Radar Applications. *Electronics* **2021**, *10*, 667. [[CrossRef](#)]
37. Govindarajulu, S.R.; Hokayem, R.; Tarek, M.N.A.; Guerra, M.R.; Alwan, E.A. Low Profile Dual-Band Shared Aperture Array for Vehicle-to-Vehicle Communication. *IEEE Access* **2021**, *9*, 147082–147090. [[CrossRef](#)]
38. Hu, H.; Lai, F.; Chen, Y. Dual-Band Dual-Polarized Scalable Antenna Subarray for Compact Millimeter-Wave 5G Base Stations. *IEEE Access* **2020**, *8*, 129180–129192. [[CrossRef](#)]
39. Wang, Y.; Wu, B.; Zhang, N.; Zhao, Y.; Su, T. Wideband Circularly Polarized Magneto-Electric Dipole 1x2 Antenna Array for Millimeter-Wave Applications. *IEEE Access* **2020**, *8*, 27516–27523. [[CrossRef](#)]
40. Javanbakht, N.; Amaya, R.E.; Shaker, J.; Syrett, B. Fixed Frequency Beam-Scanning HMSIW-Based Leaky-Wave Antenna Composed of Circular Slots in V-Shape Configuration. *IEEE Access* **2021**, *9*, 52891–52901. [[CrossRef](#)]